Iranian Journal of Science and Technology, Transactions of Electrical Engineering (2023) 47:1343–1363
https://doi.org/10.1007/s40998-023-00628-3

RESEARCH PAPER

Analysis of Arc Faults and Utility Disturbances in a Multiple Photovoltaic-Based DC Ring Microgrid by Using Improved MFDFA

Kanche Anjaiah[1] · P. K. Dash[1] · M. Sahani[1]

Received: 30 September 2021 / Accepted: 31 May 2023 / Published online: 3 July 2023

Abstract
This paper presents a new approach for arc fault and utility disturbance detection and classification in a multiple photovoltaic-based DC ring microgrid by using improved multifractal detrended fluctuation analysis (MFDFA). Initially, simulated DC faults and utility disturbances are captured from the DC microgrid, and they are processed through a cumulative sum algorithm for fault detection based on a threshold value. Thereafter, detected faults and utility disturbances are fed to the improved MFDFA for accurate fault classification. This approach consists of two stages, in the first stage, an overlap moving window-based algorithm (OMW) is implemented to divide the time scale series, and in the second stage, variational mode decomposition (VMD) is introduced for fitting a polynomial by using the best intrinsic mode functions (IMFs) of traditional MFDFA, called OMW-VMD-MFDFA. The best IMFs are selected based on the maximum value of the weighted kurtosis index, and then this approach replaces the least-square polynomial fitting method for estimating the local trends. To analyze misclassification, a total of five discriminative multifractal features are extracted from the OMW-VMD-MFDFA, and suitable combinations are plotted in a three-dimensional scatter plot. Among them, the most discriminative feature set is utilized to demonstrate the efficacy of the proposed classifier and also compared with benchmark techniques in terms of relative computational time and classification accuracy to evidence its superiority. Ultimately, the proposed approach is validated on the dSPACE DS1104 embedded processor to enable real-time testing, assessment, and validation of its simplicity, robustness, and feasibility.

Keywords PV partial shading · PV irradiation · Overlap moving window · Variational mode decomposition · Weighted kurtosis index · Arc faults · Utility disturbances · CA · RCT · dSPACE 1104

1 Introduction

Nowadays, the world's increasing population and industrial revolution have led to a surge in energy demand. Most researchers are turning their attention to renewable energy sources (RESs), such as photovoltaic (PV) and wind power, due to their abundance in nature and depletion of fossil fuel resources. Currently, there is significant research attention on low-voltage distribution networks. In particular, PV-based microgrids are emerging research areas under different conditions such as irradiation change and partial shading. Microgrids are classified as AC and DC or hybrid based on the voltage and the type of equipment connected in the network (Justo et al. 2013). DC microgrids have several advantages, such as greater reliability, better cost-effectiveness, greater power transfer capacity, no power factor losses, and better phase synchronization, as compared to AC microgrids (Saleh et al. 2018).

DC microgrids pose significant challenges in detecting and classifying arc faults and utility disturbances, particularly in bidirectional power flow systems like DC ring microgrids. To address these challenges, researchers have focused on developing protection schemes, with some proposing a differential protection scheme that can detect and classify faults with high accuracy, as evidenced by previous studies (Dhar et al. 2017; Dhar and Dash 2017; Sarangi et al. 2020). However, the implementation of this scheme necessitates a communication channel with high bandwidth capacity to facilitate the transmission of signals

✉ P. K. Dash
pkdash.india@gmail.com

[1] Siksha O Anusandhan Deemed to be University, Bhubaneswar, India

and enable effective fault monitoring. Additionally, backup protection measures are necessary to mitigate the risk of failure, which ultimately increases the complexity and cost of the grid. Despite the promising potential of the Kalman filter for detecting arc faults by estimating line admittance, the filter's accuracy and robustness have been a matter of concern (Gajula and Herrera 2020). The adaptive droop control method is performed in the DC microgrid for arc fault detection by estimating the impedance with the droop method (Augustine et al. 2020). This method is suitable for only the low impedance value, and it depends on the virtual resistance. An electromagnetic radiation signal-based detection scheme is introduced (Xiong et al. 2017) to detect arc faults by using the fractal antenna. This method needs fast switching and sensing devices to transmit the radiation from the grid to the antenna. For power quality (PQ) disturbances, detection is presented (Subasi et al. 2011; Cho et al. 2019) by using the Teager energy operator where the first peak point is considered as the fault detection point. However, Teager energy shows various peaks due to more chattering in the arc faults; as a result, the selection of threshold is difficult. In Ullah and Hanif (2021), a distribution static compensator with super-twisting sliding mode control is proposed, and it provides enough information for the detection of sag and swell but is not suitable for other PQ disturbances.

Various signal processing algorithms have recently been introduced for fault detection and classification by using target features. Well-known signal processing techniques such as S-transform (Mahela and Shaik 2017), wavelet transform (WT) (Wang and Balog 2015), discrete wavelet transform (DWT) (Yao et al. 2013), empirical mode decomposition (EMD) (Lala and Karmakar 2020), and ensemble EMD (EEMD) (Liu et al. 2015) have the demerits like dimensionality reduction, proper mother wavelet selection, mode mixing, and loss of information. In Naik et al. (2019), a kernel-based discrete time–frequency transform (KBDFT) is used to detect faults. This method is effective only if the proper kernel is selected. Although all the aforementioned methods are time–frequency based, the application of fractal analysis has garnered significant attention in recent years, owing to its numerous advantages (Das et al. 2018; Xu et al. 2019; Miao et al. 2019). Among the various methods of fractal analysis, detrended fluctuation analysis (DFA) has attained wide popularity for non-stationary signal detection. However, the DFA method suffers from the local fractal analysis, but it can deal very well with overall fractal components (Das et al. 2018). To overcome these problems, DFA and variational mode decomposition (VMD) are hybridized (Xu et al. 2019; Miao et al. 2019); as a result, the efficiency of the algorithm is improved but not sufficiently. Currently, multifractal DFA (MFDFA) analysis has been exploited for machinery vibration and biomedical signals (Prasad and Dash 2021; Chatterjee et al. 2017), because it can concern both local and overall fractals to fixed polynomials. Despite this, MFDFA still faces a few difficulties such as the estimation of scales and the order of the fitting polynomial trend; also, it is not suitable for higher-order polynomials. To resolve these issues, optimized EMD-based MFDFA and modified MFDFA named as OMW-EEMD-MFDFA are proposed (Lin et al. 2021; Zhang et al. 2019). The reliability and robustness of these algorithms mainly depend on the ensemble number.

To address the aforementioned challenges, this paper introduces a new approach for detecting and classifying arc faults and utility disturbances in multiple PV-based DC ring microgrids. Primarily, arc faults and utility disturbance signals are collected under two scenarios, such as partial shading and solar irradiation change in the proposed microgrid. These signals are fed to the cumulative sum (CUSUM) for fault detection based on any changes. Further, detected fault signals are passed through the proposed algorithm, i.e., improved MFDFA for classification. This algorithm consists of two stages: in stage 1, an overlap moving window-based algorithm (OMW) is implemented to segregate the signal into equal lengths. In stage 2, variational mode decomposition (VMD) is introduced for fitting polynomials using intrinsic mode functions (IMFs) in traditional MFDFA. In order to reduce the computational burden, the most significant IMFs are selected for estimating local trends based on the weighted kurtosis index (WKI), which can be obtained by the product the of correlation coefficient (CC_f) and kurtosis index (KI_s). The improved MFDFA is named OMW-VMD-MFDFA and is used to resolve the drawbacks of the traditional MFDFA. Therefore, the following are the main novelties and contributions of this paper:

(i) Construction of a multiple PV-based DC ring microgrid for the generation of arc faults and utility disturbances under PV irradiation change and partial shading scenarios in a MATLAB/Simulink environment.
(ii) The quick and accurate detection of the arc faults and utility disturbances, is achieved using the cumulative sum (CUSUM) method.
(iii) The novel OMW-VMD-MFDFA classifier is introduced to classify the recorded fault signals efficiently and is also used to estimate the best feature set for faults diagnosis from the three-dimensional (3-D) graphs.
(iv) To validate the efficacy of the proposed classifier, its performance is evaluated based on classification accuracy (CA) and relative computational time (RCT), and compared against existing

classifiers DFA, MFDFA, adaptive MFDFA, OMW-MFDFA, and OMW-EEMD-MFDFA.

The remainder of this paper is organized as follows: Section 2 illustrates the configuration of the proposed model and various faults. Section 3 describes fault detection using CUSUM. Section 4 illustrates the classification of arc faults and utility disturbances using the proposed OMW-VMD-MFDFA method. Section 5 presents the result analysis and the comparison of the proposed method with existing techniques. Section 6 draws the conclusion followed by future scope.

2 Multiple PV-Based DC Ring Network

In this section, the construction of a multiple PV-based DC ring microgrid in the MATLAB/Simulink software environment is described as follows: PV arrays 1, 2, and 3 are connected at buses 1, 2, and 5, respectively, as shown in Fig. 1. PV array 1 consists of four PV panels, and each panel has a rating of 100 kW. PV array 2 consists of 200 kW, and PV array 3 consists of 100 kW. To maintain the demand–supply balance, a DC lamp load with 300 kW is interfaced at bus 3. To ensure an uninterrupted power supply to the load, a 100-kW-rated battery is integrated with the DC microgrid at bus 4. Here, the battery acts as backup management equipment during islanding mode or power interruption conditions to drive the load. In grid-connected mode, the battery acts as a slack terminal to regulate the voltage and frequency levels of the microgrid (Prasad and Dash 2021; Mohanty and Pradhan 2018).

Additionally, the utility grid is connected at bus 6 with a rating of 50 MVA to ensure reliable power supply to the microgrid system. Different simulation parameters of the proposed model are included in Table 1. To simulate arc faults and utility disturbances, different load and resistance variations were taken into account in the proposed model, and they were recorded at the point of common coupling (PCC). To investigate the effects of partial shading and irradiation variations on fault current, multiple methods have been developed (Yao et al. 2013; Prasad and Dash 2021; Pragathi et al. 2020, 2021; Yao 2016), but they focus solely on the current profile. Unlike benchmark techniques, this paper focused on both voltage and current profile impact during uncertainties.

Generally, arc faults are caused by insulation failure and interconnections on bus bar cables (Dhar et al. 2017). These faults can be categorized into series arc faults and shunt arc faults, which are further segregated into intra-string and cross-string faults, and they were simulated in MATLAB/Simulink environments using Fig. 2. Currently, detecting arc faults is a key challenge, as most detection techniques fail to identify them due to their low fault current magnitude (Yao 2016).

The detection time for arc faults is usually greater than that for other faults. According to Yao et al. (2013) and

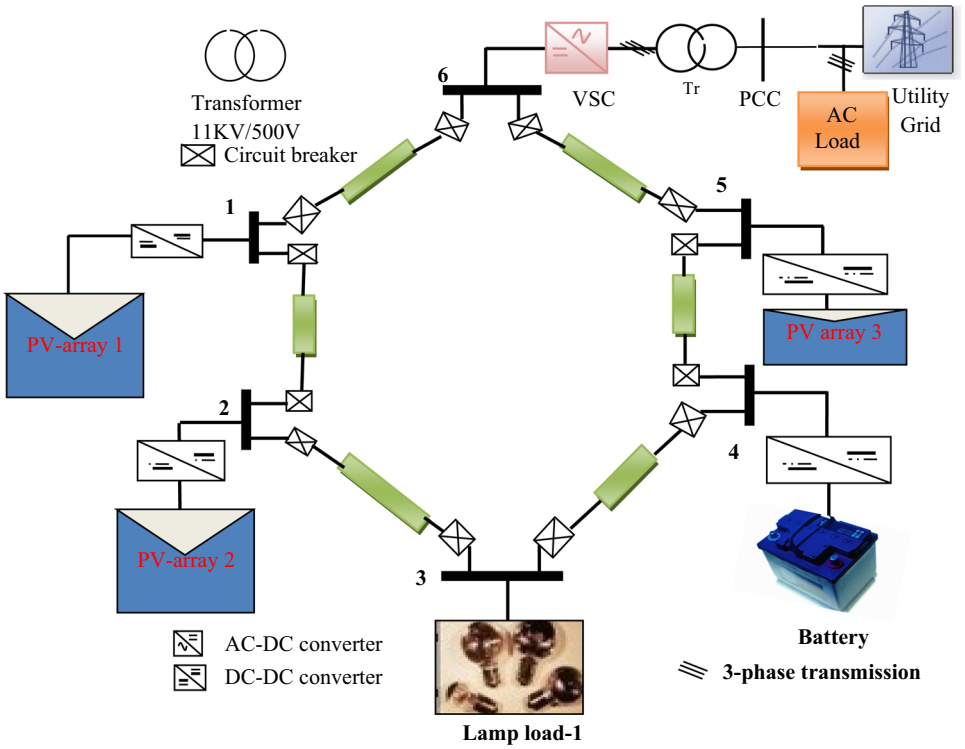

Fig. 1 Multiple PV-based DC ring microgrid

Table 1 Parameters of the proposed model

DC bus voltage	550 V
DC-link capacitor	100 μF
Parameters of PV arrays	
Photovoltaic array 1	400 kW
Photovoltaic array 2	200 kW
Photovoltaic array 3	100 kW
DC–DC converter 1	4 × 108 kW (± 8% IEC 6210)
DC–DC converter 2	2 × 108 kW (± 8% IEC 6210)
DC–DC converter 3	1 × 108 kW (± 8% IEC 6210)
Parameters of battery	
Battery	96 V, 0.4 kAh
Bidirectional DC–DC converter	150 kW, 500 V
Load and cable parameters	
DC and AC loads	DC lamp load 1 → 300 kW& AC load 2 → 150 kW,10 kvar
Cable length	2 km (i.e., bus 1–2, 2–3, 3–4, 4–5, 5–6, 6–1)
Resistance/ km	0.645 Ω/km
Inductance/ km	0.251 mH/km
Capacitance/ km	0.523 μF
AC grid side parameters	
Voltage source converter	Frequency 60 Hz, 400 kW, 260 V
Utility grid	11 kV, 50 MVA
Transformer	Tr → 11 kV/500 V

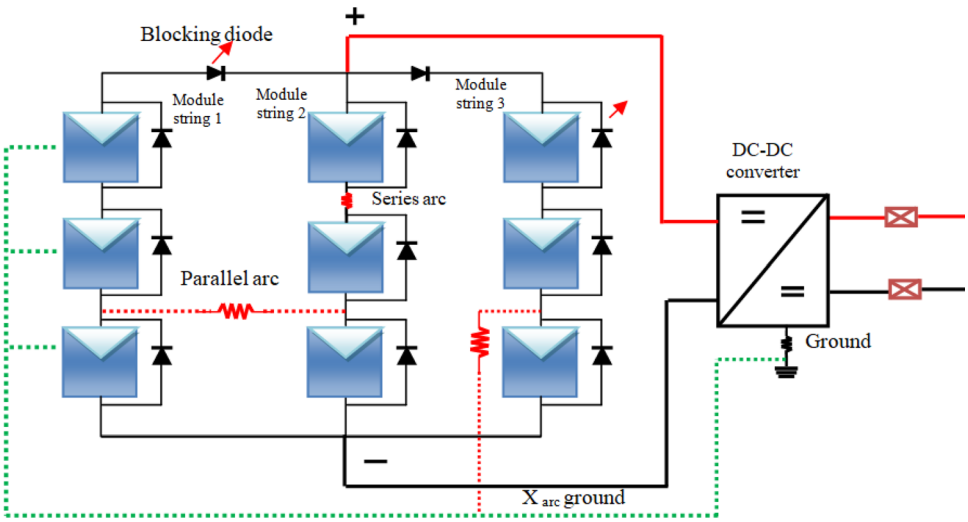

Fig. 2 Schematic diagram for arc faults in a PV array

Yao (2016), the DC arc fault is modeled as a nonlinear resistor using the revised Paukert's equation, as follows:

$$V_{\text{arc}} = \frac{m + pL}{I_{\text{arc}}^{n+qL}} \tag{1}$$

where $m, n, p, q \in R$, and L is the gap length. Through curve fitting, the method was experimentally proved for both variable and fixed gap lengths and resistance (Yao et al. 2013; Yao 2016). Experimentally, the obtained values of m, n, p, and q for the fixed gap length of 0.12 with the arc fault current less than 25A is as follows:

$$V_{\text{arc}} = \frac{20.19 + 526.5L}{I_{\text{arc}}^{0.1174+1.888L}} \tag{2}$$

Power quality disturbances occur due to nonlinear loads and sudden load changes in the DC microgrid (Wang and Balog 2015). The swell, harmonics, and transient utility disturbances are considered in this paper, because these disturbances have a greater effect if any changes occur in terms of source and load (Ullah and Hanif 2020, 2021). The considered faults are simulated under two case studies: PV irradiation change and partial shading conditions. To

extract the maximum power point from the PV modules in the proposed model, an improved perturb and observe method (IP&O) is used (Ahmed and Salam 2015). It exhibits multiple local maximum power points (LMPP) and one global MPP (GMPP) in power–voltage (P–V) and current–voltage (I–V) curves (Kurniawan and Shintaku 2020; Ahmad et al. 2017) under a partial shading condition. Among these peaks, one is the true maximum power, i.e., GMPP. Based on this parameter, maximum power is extracted from the PV array under any uncertainties of PV irradiation with the help of maximum power point tracking (MPPT) techniques. If the MPPT technique fails to detect and extract the GMPP from the PV array, then the system will operate based on the LMPP. As a result, the overall efficiency and accuracy of the system will be affected due to the suboptimal power quality at this optimum operating point. To avoid this problem, an improved P&O technique is used in the proposed work to extract the GMPP. Based on this, the GMPP fault current magnitude also changes under nonuniform conditions, i.e., partial shading, climate changes, etc. All these case studies are performed in a MATLAB/Simulink environment considering a constant temperature of 25 °C.

2.1 Modeling of PV and Battery

2.1.1 PV Modeling

A PV array converts solar energy into electrical energy. As a result, solar radiation, photovoltaic module performance, and the surrounding temperature have the most effects on the PV system's output. The temperature coefficient is taken into consideration (Dhar et al. 2017; Shaikh et al. 2022) while designing the PV array to determine its output power, which can be expressed as follows:

$$P_{PV}(t) = N_{PV} \times P_{\text{rated}}PV \times \mu_{PV} \times I_{PV}(t)[1 - \sigma_{TP}(T_S(t) - T_A(t))] \tag{3}$$

where P_{PV} (t) is the PV system's real output power, N_{PV} is the number of PV panels, P_{rated} PV is the nominal capacity of the PV array, I_{PV} is the deterioration factor, I_{PV} (t) is solar irradiation incident on the PV panel, and T_{TP} is the temperature factor, which represents the change in the output power of a PV panel with respect to its surface temperature T_s (t). The PV panel's ambient temperature in standard test conditions (25 °C) is denoted as $T_A(t)$, while the efficiency of the panel at these conditions is represented with percentage, as follows:

$$T_A(t) = \frac{T(t) + \left((T_{\text{PVnom}}(t) - 20)/\left(\frac{I_{PV}(t)}{0.8}\right)\right)\left(1 - \frac{\mu_A(1-25\sigma_{TP})}{0.9}\right)}{1 + \left(\left((T_{\text{PVnom}}(t) - 20)/\left(\frac{I_{PV}(t)}{0.8}\right)\right)(\sigma_{TP}\mu_A)/0.9\right)} \tag{4}$$

where T_{PVnom} is the PV cell nominal operating temperature (25 °C), μ_A is the efficiency at standard test conditions (%), and T (t) is the ambient temperature (°C).

2.1.2 Battery Modeling

To drive the load in the proposed model under fault scenarios or uncertainties in solar energy, a battery is necessary. Therefore, designing a battery storage system to balance the power within the ring microgrid is essential. In this paper, a DC–DC bidirectional converter is employed to connect the battery to perform charging/discharging operations in accordance with load demand. When designing a battery, mainly two parameters (Shaikh et al. 2022), i.e., battery voltage (V_{bat}) and state of charge (SOC), need to be considered, as follows:

$$V_{\text{bat}} = V_0 - R_{\text{bat}}I_{\text{bat}} - P\frac{Q_{\text{bat}}}{Q_{\text{bat}} - \int I_{\text{bat}}dt} + Ee^{(-G\int I_{\text{bat}}\text{dt}} \tag{5}$$

$$\text{SOC} = 100\left(1 - \frac{\int \text{I}_{\text{bat}}\text{d}t}{Q_{\text{bat}}}\right) \tag{6}$$

where P, G, *and* E indicate the polarization voltage, exponential capacity, and voltage, respectively, while Q, I_{bat}, R_{bat}, and V_{bat} indicate the battery capacity, current, internal resistance, and open-circuit voltage, respectively. Moreover, the charging and discharging of the battery can be modeled with respect to the state of charge (SOC) using the following equations:

$$\text{SOC}(t) = (1 - b) \times \text{SOC}(\text{t} - 1) + \left(P_{\text{gen}}(t) - P_L(t)\right)\mu_{\text{bat,charging}} \times \frac{\Delta_t}{E_{\text{bat}}} \tag{7}$$

$$\text{SOC}(t) = (1 - b) \times \text{SOC}(t - 1) - \left(P_L(t) - P_{\text{gen}}(t)\right)\mu_{\text{bat,discharging}} \times \frac{\Delta_t}{E_{\text{bat}}} \tag{8}$$

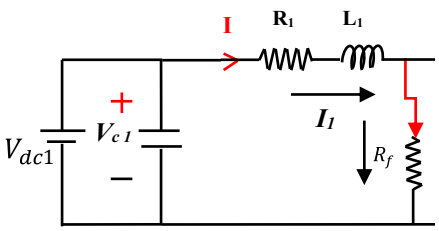

Fig. 3 Short-circuit fault

where b is a self-discharging factor (0.01), SOC(t) is the state of the battery, P_{gen} (t) is the total amount of power produced by the microgrid, P_L (t) is the total load demand, E_{bat} is the nominal capacity of the battery, $\mu_{\text{bat,charging}}$, $\mu_{\text{bat,discharging}}$ are battery efficiencies under charging/discharging modes, respectively, and Δ_t is interval time.

3 Faults Detection and Power Flow Analysis in the Proposed Model

3.1 Fault Detection Using the CUSUM Method

The cumulative sum is determined by accumulating the difference between current cycles and a reference cycle (Dhar and Dash 2017; Prasad and Dash 2021; Musa et al. 2018; Noori and Shahrtash 2013). This method shows any abrupt change present in the differential current signal of the current sample "s" as compared with the previous sample with a low computational burden. In this paper, current and voltage signals are considered under different case studies, i.e., solar irradiation change and partial shading conditions, to perform the CUSUM operation. The CUSUM method is executed in two ways: one is a sample-by-sample and the other is a window-by-window approach. In the sample-by-sample process, the current sample "s" is compared with the previous sample, i.e., "s − 1." As a result of this process, the maximum CUSUM index value is obtained under sudden variations in the signal (Prasad and Dash 2021; Musa et al. 2018). Whenever the index exceeds a threshold, that particular moment is treated as the fault detection time. In the window-based method, the total number of samples per window is considered as "w." Among three consecutive comparisons of threshold values of s^{t0}, $(s+1)^{t0}$, and $(s+2)^{t0}$ samples in both the windows of j^{t0} and $(j+1)^{t0}$, which has the maximum detection index is considered as the fault detection time at that particular time instant. CUSUM provides faster fault detection and the positive values of their results, irrespective of the nature of polarity of the input signal, i.e., differential current signal (I_{d}).

Here $s = 1, 2, 3 \cdot w$ and $j = 1, 2, 3 \cdot j$.

The number of windows is computed as $j_2 = x/j$

$$\text{CUSUM}\ (s) = \ \text{CUSUM}\ (s-1) + I_d(s) - I_d(s - \lambda N_s) \tag{9}$$

where N_s, I_d , s, and λ indicate the number of samples/window, differential current, an instant of a sample, and positive integer (considered as unity), respectively.

If CUSUM > CUSUM_threshold

trip flag == 1;

$$\text{CUSUM detection time} = (\text{CUSUM}\ (s) - \ \text{CUSUM}\ (s_1)) \times T_s \tag{10}$$

where T_s indicates the time interval between samples, CUSUM_threshold is determined at an instant of j^{th} through a trial and error method, and the first instant that the CUSUM index goes over zero is denoted as s_1.

3.2 Short-Circuit Faults and Power Flow Analysis

3.2.1 Short-Circuit Analysis

In the proposed model, the short-circuit fault is shown in Fig. 3

Apply the Kirchhoffs voltage law (KVL) for the Fig. 3:

$$V_{c1} = I_1(R_1 + R_{\text{f}}) + L_1 \frac{\text{d}I_1}{\text{d}t} \tag{11}$$

where

$$V_{dc1} = \text{V}_{\text{c1}} = \frac{1}{C}\int I_1 \text{d}t$$

By considering the fault instant at time t_0, the RLC response of the circuit, which consists of resistance (R), inductance (L), and capacitance (C), can be represented in the frequency domain as follows:

$$I_1(s) = \frac{\frac{V_{c1}(0)}{L_1} + sI_{L1}(0)}{s^2 + s\frac{R_1+R_f}{L_1} + \frac{1}{L_1 C_1}} \tag{12}$$

where V_{c1} (0), I_{L1} (0) are the voltage across the capacitors and currents flowing through the inductor, respectively, just before the fault occurrence. In Eq. (12), the converter contribution to the fault is neglected due to slow response, and its time domain can be obtained by considering the underdamped response as follows:

$$I_1 = \frac{V_{c1}(0)}{L_1\omega_{d1}} e^{-\alpha_1 t} sin(\omega_{d1} t) + I_L(0) e^{-\alpha_1 t}\left[\cos(\omega_{d1} t) - \frac{\alpha_1}{\omega_{d1}} sin(\omega_{d1} t)\right] \tag{13}$$

where

$$\omega_{d1} = \sqrt{\omega_n^2 - \alpha_1^2}; \omega_n = \frac{1}{\sqrt{L_{\text{ieq}} C_{\text{i}}}}, \alpha_1 = \frac{R_1 + R_f}{2L_1}$$

The initial voltage across the converter filter capacitance is the most significant factor shaping the fault current profile, due to the combination of high filter capacitance and low cable inductance. This results in a significant impact on underdamped fault current characteristics, as

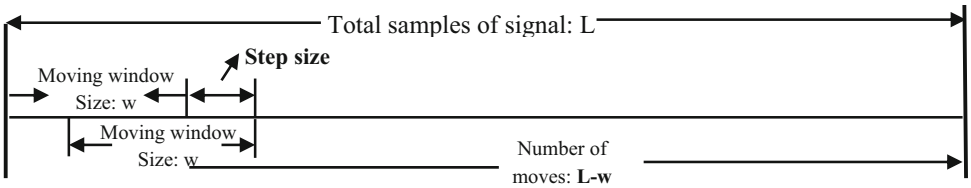

Fig. 4 Overlap moving window architecture

illustrated in Eq. (13), which can be used to represent the fault current profile, as follows:

$$I_1(t) = \frac{V_{c1}(0)}{L_1 \omega_{d1}} e^{-\alpha_1 t} sin(\omega_{d1} t). \tag{14}$$

3.2.2 Power Flow Analysis in the Proposed Model

To investigate the steady-state characteristics of the proposed microgrid before and after a fault is crucial. As a result, understanding the consequences of faults becomes more complex. For this purpose, power flow computation, which does not require simulations (Yao et al. 2013; Yao 2016), is the most suitable method for achieving this goal.

Assuming the total number of buses in the proposed model is n (where $n = 6$), according to Kirchhoff's current law, the current injected at the bus i is equal to the sum of current flowing through other n-1 buses.

$$I_i = \sum_{\substack{j=1 \\ j \neq i}}^{n} Y_{ij}(V_i - V_j) \tag{15}$$

where Y_{ij} refers to the admittance between two buses (i and j), while V_i and V_j denote the voltage magnitudes at those respective buses. Admittance can be obtained using impedance (Z), and it can be estimated by $[V_{dc1}] = [I_1][Z]$

Finally, the power flow equations for any bus can be calculated as follows:

$$P_i = V_i I_i \tag{16}$$

From Eqs. (15) and (16),

$$P_i = V_i \sum_{\substack{j=1 \\ j \neq i}}^{n} Y_{ij}(V_i - V_j) \tag{17}$$

According to the load and power in the proposed model, the power flow equation is as follows:

$$P_L = P_{\text{grid}} + PV_1 + PV_2 + PV_3 \pm P_{\text{bat}} \tag{18}$$

where P_L is load demand, PV_1, PV_2, and PV_3 are the PV array's output power, and $\pm P_{\text{bat}}$ represents the battery output power in charging/discharging modes.

4 Fault Classification Using the Proposed Algorithm

The proposed OMW-VMD-MFDFA algorithm has two stages. In stage 1, an overlap moving window-based algorithm (OMW) is implemented to segregate the signal into the equal length of windows (Zhang et al. 2019). In stage 2, variational mode decomposition (VMD) is introduced for fitting polynomials by estimating the local trends with the help of IMFs in classic MFDFA.

4.1 Overlap Moving Window (OMW)

To address the issue of discontinuity in data segmentation, the OMW-based algorithm is utilized; by estimating the moving window size (Zhang et al. 2019) from the fault signal of length L and determining the step size (s) for each iteration. Here, the algorithm iterates through the signal for a number of iterations that depends on the signal length or total samples, as shown in Fig. 4, and it can be calculated as follows:

$$\text{Total number of iterations} = \text{total length } (L) - \text{window size } (w)$$

4.2 Variational Mode Decomposition (VMD)

The popular VMD technique has been used by signal processing enthusiasts all over the world to break down nonlinear signals into several sub-signals (μk), also referred to as intrinsic mode functions (IMFs) (Xu et al. 2019; Miao et al. 2019). Each mode is connected to a central frequency (ωk) by means of the |^2 norm, and its bandwidth is evaluated via the gradient estimate (Lin et al. 2021; Isham et al. 2018). As a result, VMD is characterized by both equality and inequality constraints, posing an optimization challenge in the form of the following equation:

$$\min_{\{k\},\{\omega_k\}} \left\{ \sum_k \left\| (\partial_t [\left(\delta(t) + \frac{j}{\pi t} \right) * \mu_k(t)] e^{-j\omega_k t} \right\|_2^2 \right\} \tag{19}$$

$$\text{subjected to} \sum_{k=1}^{K} \mu_k = \mu$$

where $\delta(t)$ indicates the Dirac distribution, $\|.\|_2^2$ indicates the L^2-norm, K is the modal number, μ is the reconstructed signal, and * indicates the convolution operator.

By incorporating the Lagrange multiplier (λ) and the fidelity factor (σ), it is possible to transform Eq. (19) into an unconstrained optimization problem. The fidelity factor reduces Gaussian noise and enhances accuracy, and the resulting augmented Lagrangian (L) is as follows:

$$L(\{\mu_k\},\{\omega_k\},\lambda) = \sigma\sum_k \left\|\partial_t\left[\left(\delta(t)+\frac{j}{\Pi_t}\right)\times\mu_k(t)\right]e^{-j\omega_k t}\right\|_2^2 + \left\|\mu(t)-\sum_k\mu_k(t)\right\|_2^2 + \langle\lambda(t),\mu(t) - \sum_k\mu_k(t)\rangle \tag{20}$$

where angle brackets ⟨⟩ represent the inner product of two variables. Equation (20) yields the best solution through an alternate direction multiplier approach, which also enables the extraction of the bandwidth of each finite mode. To upgrade the modes $(\widehat{\mu}_k^{n+1})$ and center frequencies (ω_k^{n+1}), the process employs two loops, represented as follows:

$$\widehat{\mu}_k^{n+1}(\omega) = \frac{\widehat{\mu}(\omega) - \sum_{i\neq k}\widehat{\mu}_i^n + \frac{\widehat{\lambda}^n(\omega)}{2}}{1+2\alpha(\omega-\omega_k^n)} \tag{21}$$

$$\omega_k^{n+1} = \frac{\int_0^\infty \omega\left|\widehat{\mu}_k^n(\omega)\right|^2 d\omega}{\int_0^\infty\left|\widehat{\mu}_k^n(\omega)\right|^2 d\omega} \tag{22}$$

By examining Eqs. (21) and (22), it is evident that both modes and central frequencies are upgraded, resulting in an upgraded Lagrange multiplier $(\widehat{\lambda}^{n+1})$ expressed as follows:

$$\widehat{\lambda}^{n+1}(\omega) = \widehat{\lambda}^n + \tau\left(\widehat{\mu}(\omega) + \sum_{k=1}^K \widehat{\mu}_k^{n+1}(\omega)\right) \tag{23}$$

where τ indicates the tolerance parameter.

From the earlier discussion, it is clear that as long as the convergence condition [i.e., in Eq. (24)] is not fulfilled, the process in VMD will be repeated using Eqs. (20) to (23). Once the condition is satisfied, the algorithm stops the decomposition process.

$$\sum_{k=1}^K \frac{\|\widehat{\mu}_k^{n+1}-\widehat{\mu}_k^n\|_2^2}{\|\widehat{\mu}_k^n\|_2^2} < \boldsymbol{\varepsilon} \tag{24}$$

where ε is the convergence decisive factor.

To enhance accuracy and reduce computational complexity, optimal IMF selection is crucial among a series of IMFs. It means that IMFs that contain very low noise and more information regarding the fault need to be selected. Here, the selection of the optimal IMF is based on the maximum value of the weighted kurtosis index (WKI), which is illustrated in the following section.

4.3 Weighted Kurtosis Index

All the IMFs produced by VMD do not carry much more information regarding the input signal. In this paper. the weighted kurtosis index is used (Miao et al. 2019; Gu et al. 2020) to eliminate the noise content and IMFs carrying limited information. The WKI is the product of two major indices, such as correlation coefficient (CC_f) and the kurtosis index (KI_s). Here, the KI_s is used to eliminate the higher amplitude of scattering distribution, and the CC_f is used to measure the similarity between the two-time series signals.

$$\mathrm{WKI} = |\mathrm{KI}_s| \times \left|\mathrm{CC}_f\right| \tag{25}$$

$$\text{where } \mathrm{KI}_s = \frac{\frac{1}{N}\sum_{t=0}^{N-1} S^4(t)}{\left(\frac{1}{N}\sum_{t=0}^{N-1} S^2(t)\right)^2} \text{ and } \mathrm{CC}_f = \frac{E[(S-\overline{S})(Z-\overline{Z})]}{E[(S-\overline{S})^2(Z-\overline{Z})^2]}$$

where N, Z, and $S(t)$ denote the length of the signal, IMF of the signal, and time series signal, respectively. The best three IMFs are selected among the series of IMFs using a threshold (Gu et al. 2020). In this work, after observing several simulations, the threshold is fixed as greater than two, because the IMFs below the threshold value contain more noise and less fault information.

4.4 Traditional MFDFA

MFDFA is the extension of the DFA approach, which addresses the limitations of DFA, such as local fractal analysis in nonstationary signals (Zhang et al. 2019; Martínez et al. 2021). The MFDFA algorithm is utilized to analyze the fault signals that have been previously detected using the CUSUM method.

Step 1: The profile can be subtracted from the input signal's mean in MFDFA to eliminate a specific set of components:

$$M(p) = \sum_{t=1}^p \left(X(t)-\overline{X}(t)\right), p = 1,2,\ldots,L \tag{26}$$

where L, $X(t)$, and$\overline{X}(t)$ indicate sample total, input signal, and its mean, respectively.

Step 2: The resultant signal is represented by $M(p)$, which is subdivided into L_s windows. Each window consists of non-overlapping segments with equal lengths (s):

where

$$L_s = L/s. \tag{27}$$

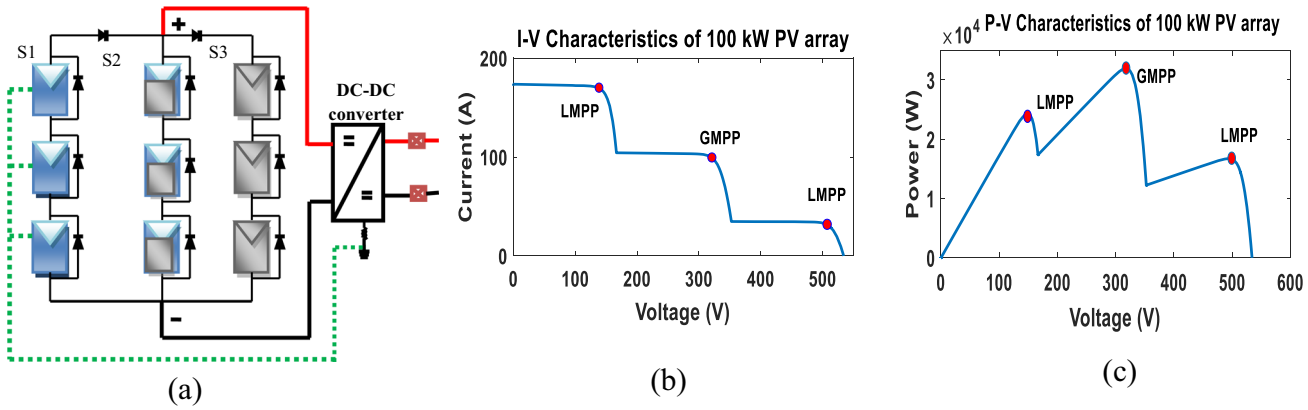

Fig. 5 Partial shading effect during **a** 100-kW PV array model. **b** I–V characteristics. **c** P–V characteristics

The above segmentation process will perform very well until the window lengths are equal. In the uncertainty condition, some part of the profile remains unused, and that will be wasted. To avoid that kind of situation, the above procedure is performed in reverse order.

Step 3: Estimate the local trends of each $2L_s$ segment, and the detrended time series Y_t (i) can be obtained as follows:

$$Y_t(i) = v_t(i) - p_t(i) 1 < i < s$$

where $v_t(i)$ and $p_t(i)$ denote the segment and trend time series data, respectively.

Step 4: The least-squares polynomial fitting method is used to calculate the local trends of each segment, enabling the estimation of the MFDFA local trends. Following this, the variance of each signal is computed, as demonstrated below:

$$F^2(s,v) = \frac{1}{n}\sum_{p=1}^{n}\{M[(v-1)s+p] - m_v(p)\}^2, \text{ for } v = 1,2,\ldots,L_s \tag{28}$$

$$F^2(s,v) = \frac{1}{n}\sum_{p=1}^{n}\{M[L-(v-1)s+p] - m_v(p)\}^2, \text{ for } v = L_s+1,\ldots,2L_s \tag{29}$$

where $m_v(p)$ is the fitted least-square polynomial, which can take the shape of a linear, quadratic, cubic, or higher-order polynomial in terms of v. The fluctuation function can be computed as follows:

$$\begin{cases} F_q(s) = \sqrt[q]{\frac{1}{2L_s}\sum_{v=1}^{2L_s} F^2(s,v)^{0.5q}} & \text{if } q \neq 0 \\ F_q(s) = exp\left\{\frac{1}{4L_s}\sum_{v=1}^{2L_s}\ln\left[F^2(s,v)\right]\right\} \approx n^{H(0)} & \text{if } q = 0 \end{cases} \tag{30}$$

where q is the polynomial order; if q = 2, then the MFDFA acts as a DFA.

Step 5: The power-law relationship is computed between the fluctuation function $F_q(s)$ and s scales as follows:

$$F_q(s) \propto s^{H(q)} \tag{31}$$

From Eq. (29), it is clear that the fluctuation function and scaling component exhibit a linear relationship. By definition, the Hurst exponent $H(q)$ is calculated for any value of q. If q = 2, then it is known as the generalized

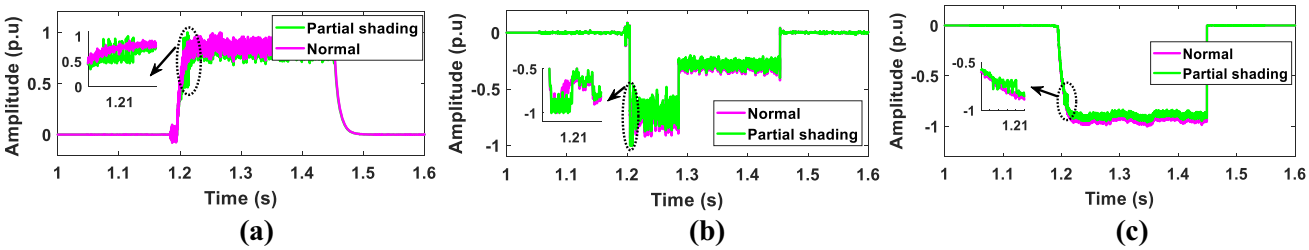

Fig. 6 Comparative results for different arc faults during unshaded (normal) and partial shading conditions: **a** series arc fault; **b** shunt cross-string fault; and **c** shunt intra-string fault

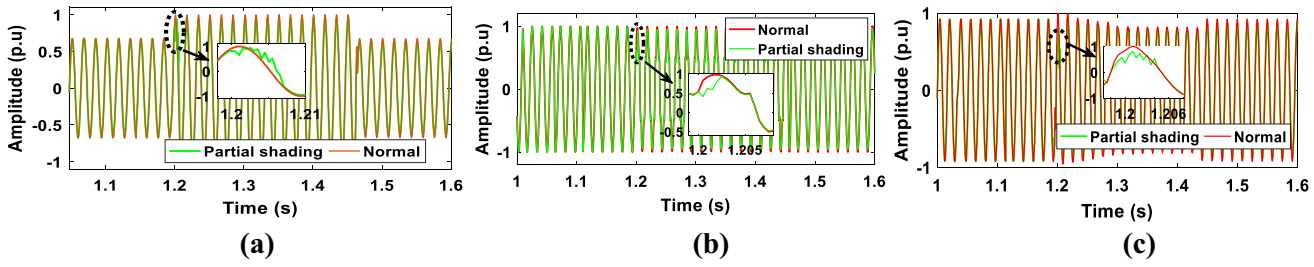

Fig. 7 Comparative results for different arc faults during unshaded (normal) and partial shading conditions: **a** swell; **b** harmonics; and **c** transients

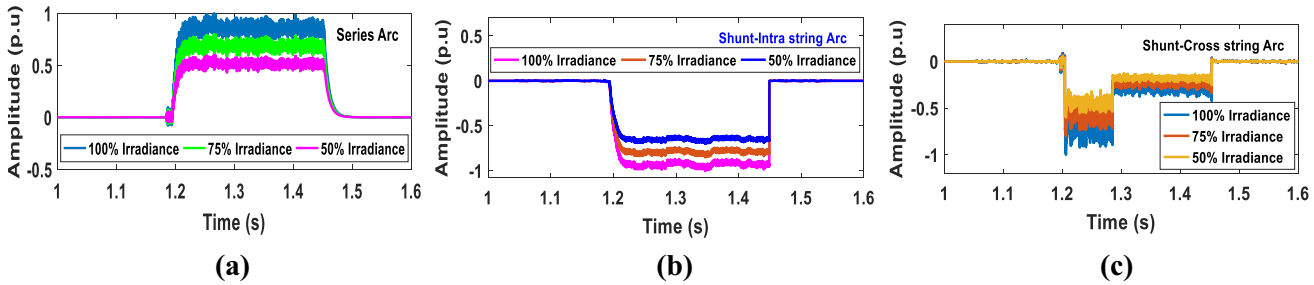

Fig. 8 Effect of PV irradiation change on arc faults: **a** series arc fault; **b** shunt intra-string arc fault; and **c** shunt cross-string arc fault

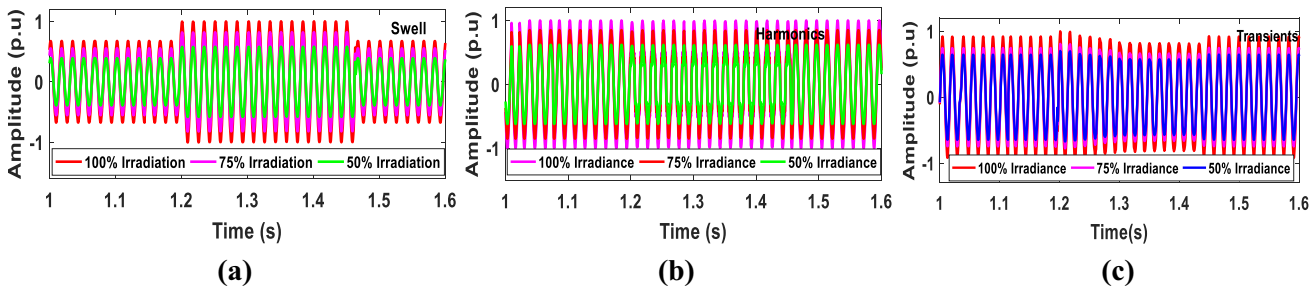

Fig. 9 Effect of PV irradiation change on utility disturbances: **a** swell; **b** harmonics; and **c** transients

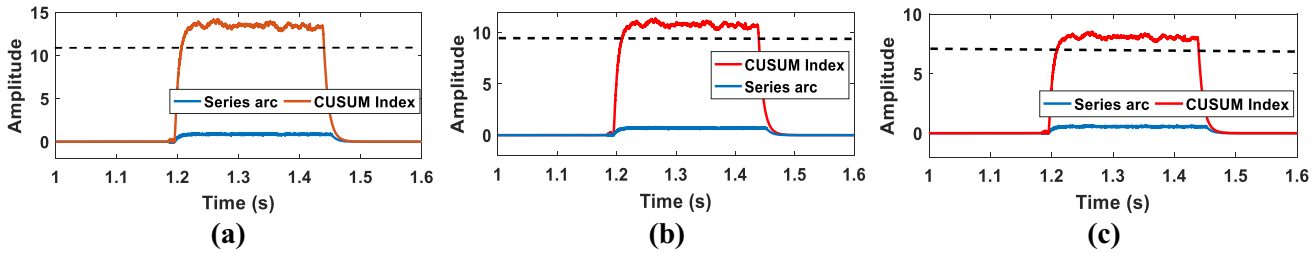

Fig. 10 Series arc fault detection using the CUSUM method under different solar irradiation levels: **a** 100% irradiation; **b** 75% irradiation; and 50% irradiation

Hurst exponent (Prasad and Dash 2021). The presence of multifractal characteristics in fault signal data can be determined by the relationship between H_q and q (Anjaiah et al. 2022a). If the variables are independent, then multifractal characteristics are absent, but if they are dependent, then multifractal characteristics are present. Moreover, a positive value for both H_q and q implies a large scaling performance of segment fluctuations, while both negative values indicate a lower scaling behavior.

Step 6: The relation between mass exponent (M_q) and Hurst exponent (H_q) is expressed as

$$M_q = qH_q - 1 \tag{32}$$

In the case of monofractal analysis, a single Hurst exponent with a mass exponent shows linear properties. In

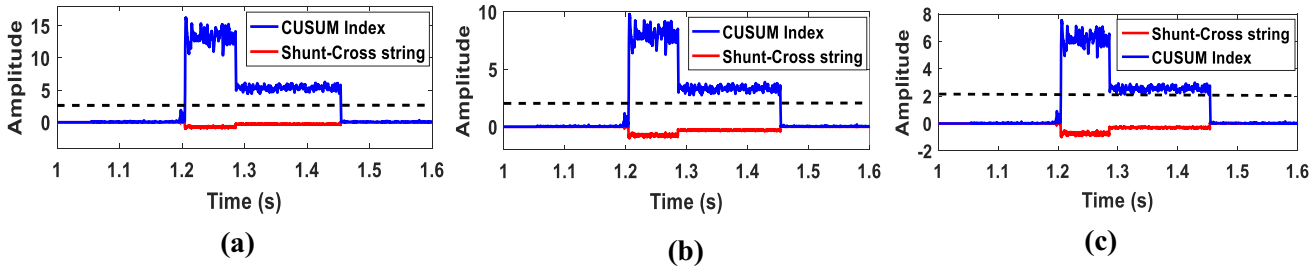

Fig. 11 Shunt cross-string arc fault detection using the CUSUM method under different solar irradiation levels: **a** 100% irradiation; **b** 75% irradiation; and **c** 50% irradiation

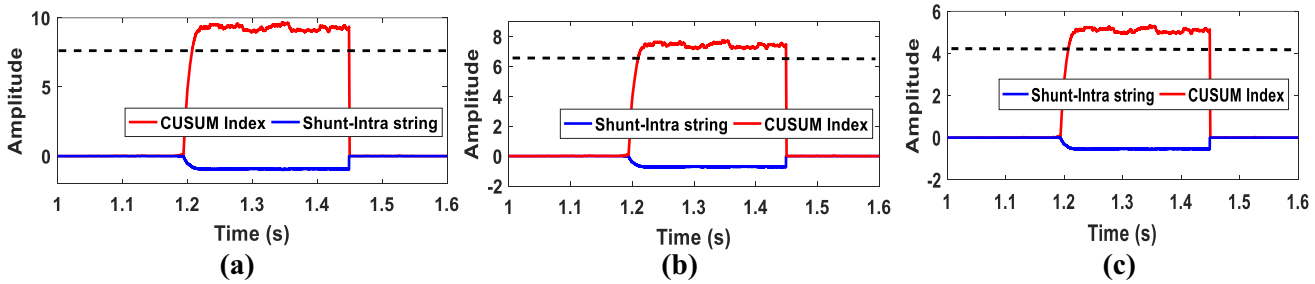

Fig. 12 Shunt intra-string arc fault detection using the CUSUM method under different solar irradiation levels: **a** 100% irradiation; **b** 75% irradiation; and **c** 50% irradiation

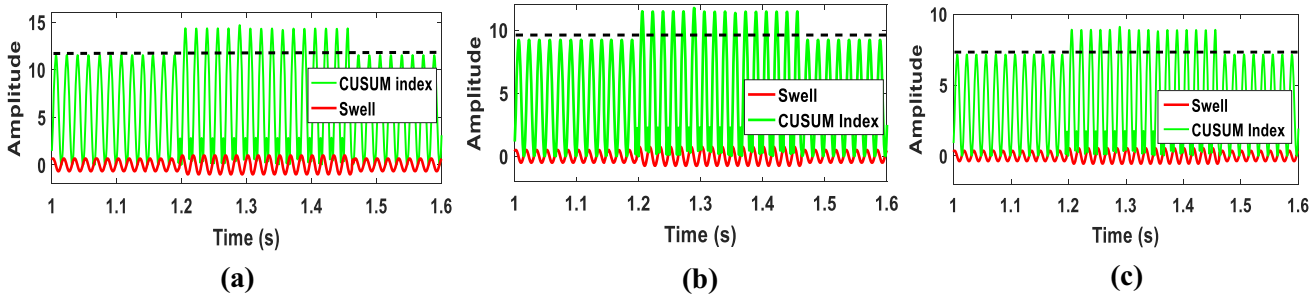

Fig. 13 Detection of swell using the CUSUM method under different solar irradiation levels: **a** 100% irradiation; **b** 75% irradiation; and **c** 50% irradiation

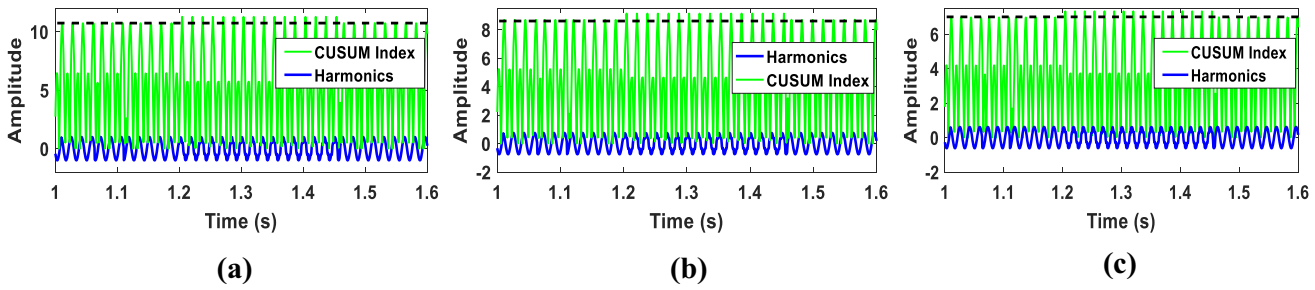

Fig. 14 Detection of harmonics using the CUSUM method under different solar irradiation levels: **a** 100% irradiation; **b** 75% irradiation; and **c** 50% irradiation

multifractal analysis, multiple Hurst exponents with a mass exponent indicate nonlinear properties.

Step 7: The Legendre transform is used to express the relationship between the mass exponent and the singularity spectrum (Sq):

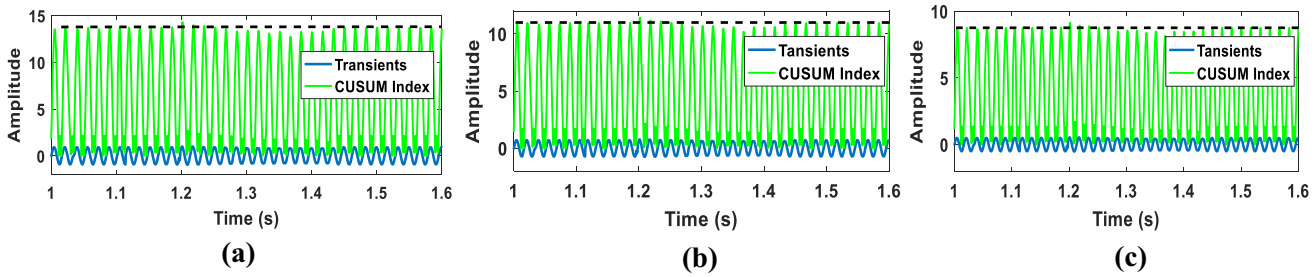

Fig. 15 Detection of transients using the CUSUM method under different solar irradiation levels: **a** 100% irradiation; **b** 75% irradiation; and **c** 50% irradiation

Table 2 Arc fault and utility disturbance detection using the CUSUM method

Type of fault	Average detection time (ms)
Shunt intra-string	11.01
Shunt cross-string	12.87
Series arc	12.31
Swell	10
Harmonics	13.27
Transients	9.68

$$\delta_q = \frac{dM_q}{dq} \tag{33}$$

$$S_q = q\delta_q - M_q \tag{34}$$

where δ_q is the singularity exponent, and S_q is also known as the fractal dimension.

$$\delta_q = H_q + qH'_q \tag{35}$$

$$S_q = q\left[\delta_q - H_q\right] + 1 \tag{36}$$

An inverted parabolic shape characterizes the multifractal spectrum, and the width of this shape corresponds to the degree of multifractality. Thus, an increase in the width of the spectrum implies an increase in the level of multifractality.

4.5 Analysis of Improved OMW-VMD-MFDFA Algorithm

Modified MFDFA algorithms, i.e., OMW-EEMD-MFDFA (Zhang et al. 2019) and adaptive MFDFA (Martínez et al. 2021), are proposed to avoid the complexities in the basic MFDFA, and it experimentally proved its accuracy in the application of precipitation analysis (Zhang et al. 2019). However, this method has a few drawbacks due to the EEMD algorithm, such as the selection of ensemble number and noise amplitude. To address those limitations, this paper introduces an OMW-VMD-MFDFA approach, and it is developed by modifying the two steps, i.e., steps 2 and 4 in the traditional MFDFA without changing other steps. In step 2, the profile is divided into equal lengths of windows without overlapping each other. The problem in this step is due to polynomial fitting, as a result of this discontinuity in the segmentation process. In order to enhance the segmentation of the fault signal data in step 2, an overlap moving window-based algorithm has been implemented in this paper. This algorithm effectively resolves the issues previously faced, and the traditional MFDFA only requires modifications in steps 2 and 4 without any impact on other steps.

Step 2: The OMW algorithm divides the profile into $L - s + 1$ overlapping segments of equal length s.

Step 4: Using the OMW algorithm, the original fault signal data is segregated into $L - s + 1$ segments, allowing the qth order fluctuation function to be calculated using the obtained segments:

$$\begin{cases} F_q(s) = \sqrt[q]{\dfrac{1}{2(L-s+1)}\sum_{v=1}^{L-s+1} F^2(s,v)^{0.5q}} & \text{if } q \neq 0 \\ F_q(s) = exp\left\{\dfrac{1}{2(L-s+1)}\sum_{v=1}^{L-s+1} \ln\left[F^2(s,v)\right]\right\} \approx n^{H(0)} & \text{if } q = 0 \end{cases} \tag{37}$$

Basic MFDFA typically assumes that local trends can be modeled as polynomials. To further refine this process, MFDFA has been incorporated with the VMD algorithm and utilizes the optimal IMFs to fit the polynomial and accurately estimate the local trends. We change step 3 without changing other steps:

$$Y_t(i) = v_t(i) - R_n(i) 1 < i < s \tag{38}$$

where $Y_t(i)$ is the time series of the fault signal. Note that the trend $R_n(i)$ should be determined for each $2L_s$ segment on time scale s.

4.6 OMW-VMD-MFDFA Feature Extraction Analysis

It is necessary to select the features to classify the faults and power quality disturbances efficiently. From the

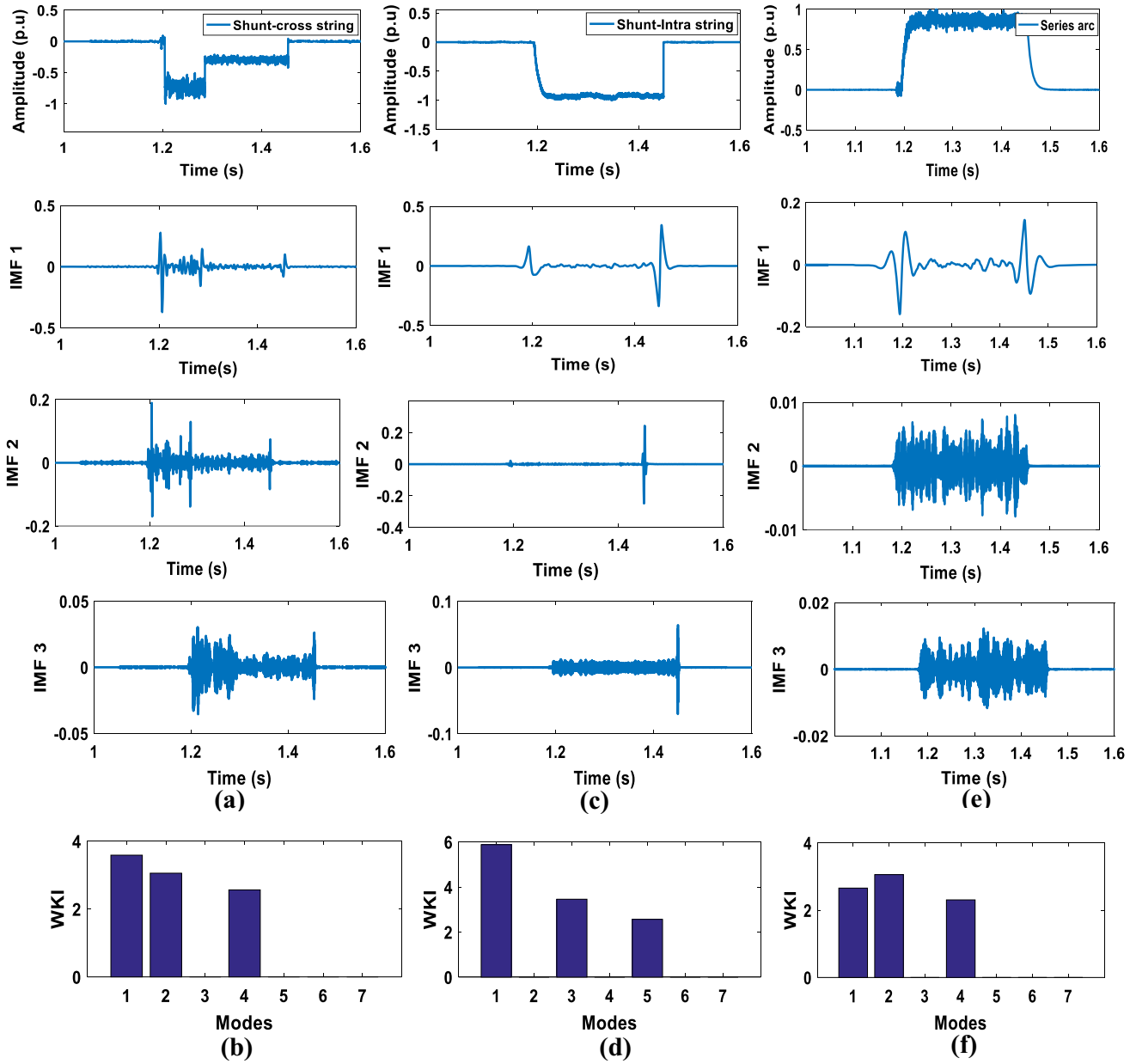

Fig.16 IMFs produced by VMD for different arc faults: **a** series arc fault and its significant IMFs; **b** WKI values for significant IMFs; **c** shunt intra-string arc fault and its significant IMFs; **d** WKI values for significant IMFs; **e** shunt cross-string arc fault and its significant IMFs; and **f** WKI values for significant IMFs

various kinds of literature, the following features are considered for fault classification.

(i) Hurst exponent (*Hq*)
(ii) Singularity spectrum (*Sq*)
(iii) The right extremity of the singularity exponent (δ_{max})
(iv) Singularity spectrum peak value (δ_{peak})
(v) Singularity spectrum width ($\Delta\delta_q$)

The abovementioned features are computed for all the simulated faults. Hurst exponent (Hq) for $q = 2$ exhibits self-affinity. The right extremity of the singularity exponent (δ_{max}) and singularity spectrum peak value (δ_{peak}) signifies the maximum fluctuation of fault signal and peak fluctuation of fault signal data, respectively. Singularity spectrum width ($\Delta\delta_q = \delta_{min}$—$\delta_{max}$) indicates the degree of the signal; higher fluctuations are represented by a wide spectral width and vice versa.

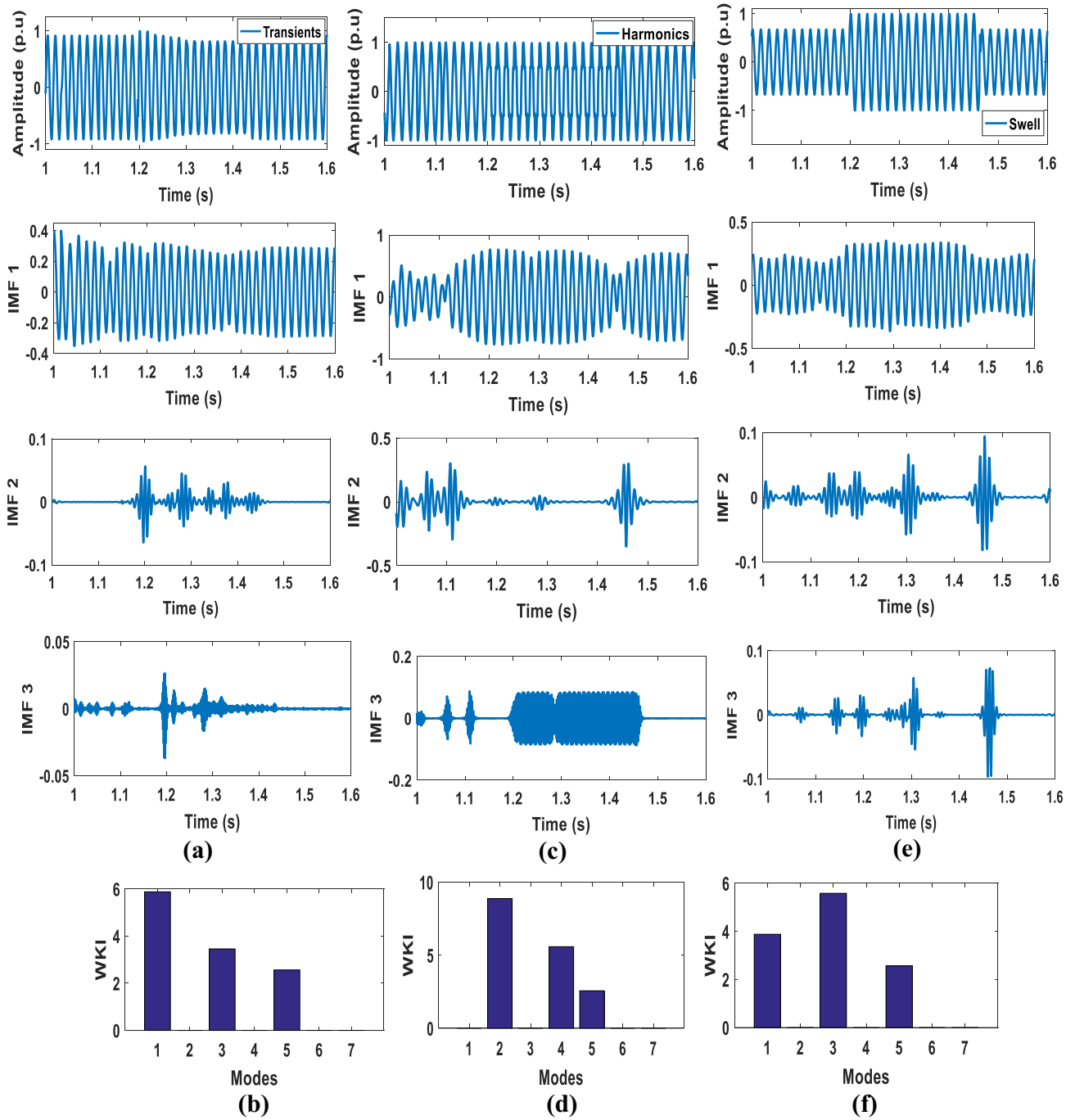

Fig.17 IMFs produced by VMD for utility disturbances: **a** swell and its significant IMFs; **b** WKI values for significant IMFs; **c** harmonics and their significant IMFs; **d** WKI values for significant IMFs; **e** transients and their significant IMFs; and **f** WKI values for significant IMFs

5 Result Analysis

Initially, various DC faults are created in the proposed model (i.e., multiple PV-based DC ring microgrid), and their corresponding signals are captured from the PCC and DC bus. Simulated faults include series arc, shunt arc (intra-sting and cross-string) faults, and utility disturbances (i.e., swell, harmonics, and transients). The effects of the simulated fault signals are investigated under two cases, such as solar irradiation change and partial shading conditions. Thus, the results indicate that the current profile in the proposed microgrid is more influenced by arc faults than the voltage profile. Similarly, utility disturbances impact the voltage more as compared to the current. Thus, both voltage and current signals are considered for fault analysis. Among six faults, three are related to arc faults,

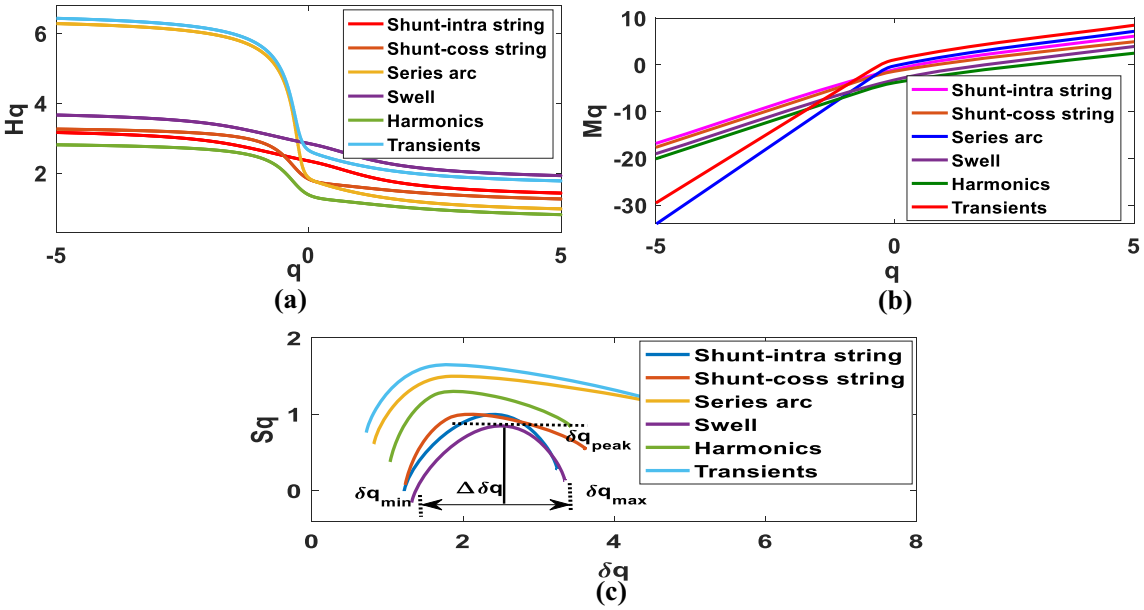

Fig. 18 Arc faults and power quality disturbances analysis by OMW-VMD-MFDFA: **a** Hurst exponent (*Hq*); **b** mass exponent (*Mq*); and **c** singularity spectrum (*Sq*)

Table 3 Feature extraction for simulated faults using the OMW-VMD-MFDFA method

Type of fault	Fault class	*Hq*	Sq	δ_{max}	δ_{peak}	$\Delta\delta_q$
Shunt intra-string	CL_1	3.784	0.272	3.415	2.307	2.213
		3.686	0.201	3.397	2.154	2.251
		3.561	0.182	3.392	2.087	2.191
Shunt cross-string	CL_2	3.249	0.377	5.782	1.819	4.925
		3.195	0.346	5.705	1.794	4.864
		3.001	0.324	5.678	1.788	4.825
Series arc	CL_3	6.486	0.852	3.384	2.647	1.987
		6.402	0.832	3.279	2.578	1.981
		6.381	0.811	3.255	2.452	1.978
Swell	CL_4	3.852	0.478	3.557	1.925	2.748
		3.815	0.461	3.527	1.901	2.729
		3.786	0.445	3.492	1.892	2.717
Harmonics	CL_5	3.186	0.611	3.957	1.789	2.925
		3.015	0.592	3.876	1.781	2.856
		2.987	0.575	3.825	1.778	2.807
Transients	CL_6	4.396	1.152	5.887	1.895	5.331
		4.185	1.027	5.759	1.882	5.287
		4.034	0.921	5.639	1.879	5.054

and the other three are related to utility disturbances. The effect of these faults under two case studies, i.e., PV partial shading and irradiation change, is presented in this paper.

5.1 Case 1: Partial Shading Effect

Generally, a partial shading effect will occur in PV arrays due to clouds, and therefore some of the modules are not exposed to sunlight (2020; Ahmad et al. 2017). Due to this phenomenon, voltage and current are influenced more, and the shaded modules produce less current and voltage than unshaded modules. This paper investigates the effects of partial shading on a 100-kW-rated PV array, which is made up of three strings with individual ratings of 33.4 kW. The experimental simulation includes three irradiation levels: fully shaded (150 W/m^2), partially shaded (600 W/m^2), and unshaded (1000 W/m^2), as depicted in Fig. 5a. The partial shading effect commences after 1.2 s in the proposed

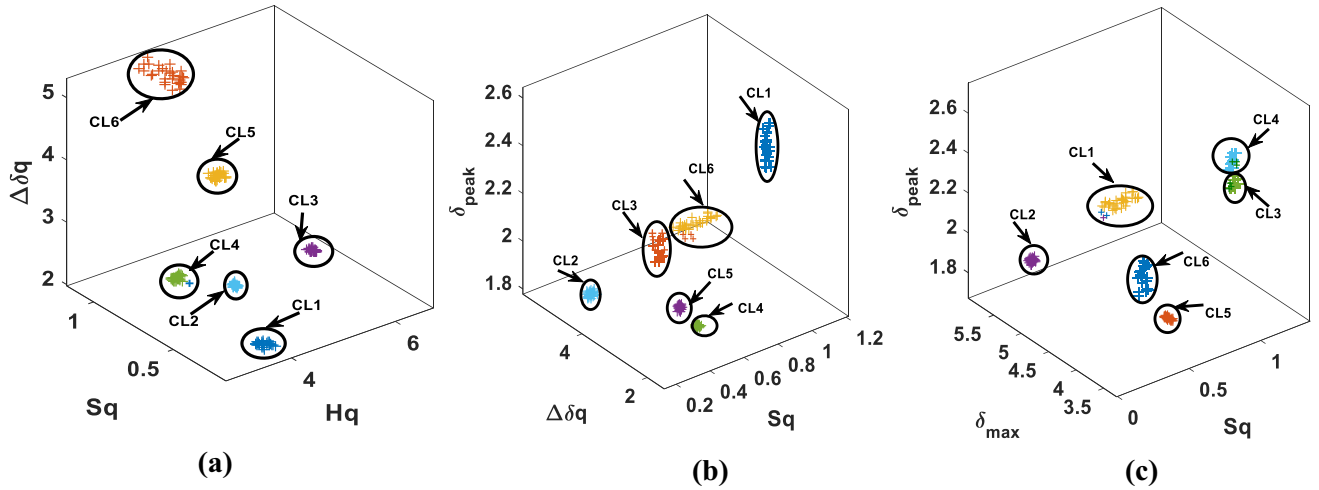

Fig. 19 Fault and utility disturbance classification in three dimensions with different features of OMW-VMD-MFDFA combination

Table 4 Classification accuracy of extracted feature sets

Features and their combination set		CA (%)
Feature set 1	Hq, Sq, $\Delta\delta_q$	**99.33**
Feature set 2	Sq, $\Delta\delta_q$, δ_{peak}	96.66
Feature set 3	Sq, $\Delta\delta_q$, δ_{max}	92.12

Bold value indicates superiority when compared to other sets

Table 5 Performance comparison of proposed and existing classifiers for nonlinear fault analysis

Classifier	CA (%)	RCT
DFA (Das et al. 2018)	97.8	2.03
MFDFA (Prasad and Dash 2021)	98.15	1.85
ADAPTIVE MFDFA (Martínez et al. 2021)	99.11	1.31
OMW-MFDFA (Zhang et al. 2019)	99.02	1.72
OMW-EEMD-MFDFA (Zhang et al. 2019)	99.17	1.18
Proposed (OMW-VMD-MFDFA)	**99.33**	**1**

Bold values indicate superiority when compared to other techniques

microgrid. During this phenomenon, two LMPPs and one GMPP are extracted using an IP&O method, and they are depicted in Fig. 5b and c.

The impact of partial shading on arc faults and utility disturbances is more pronounced than in unshaded or normal conditions, as demonstrated in Fig. 6. Analysis of the figure reveals that the effects of partial shading become apparent after 1.2 s. This is due to the differential nature of the fault current signals, which result in zero readings prior to this time. The arc fault currents are immediately high when compared with an unshaded condition, because at this instant of time, the PV array is switched to the partial shading operation. This phenomenon can be observed from the selected portion in Fig. 6. Similarly, the effect of voltage in utility disturbances under normal conditions and partial shading conditions is shown in Fig. 7. From these figures, it is clear that the voltage magnitude is the same for all the figures before the partial shading effect at 1.2 s. After 1.2 s, the source power is decreased due to partial shading. For this reason, the voltage magnitude fluctuates a little more; but after a few milliseconds, the voltage amplitude is stabilized, and it follows the unshaded voltage profile with a very low difference, because of battery action.

5.2 Case 2: Irradiation Change in the PV Array

In this scenario, the effect of solar irradiation change in the 400-kW PV array is observed in arc faults and utility disturbances. In this paper, three variations of 100%, 75%, and 50% are considered for all considered faults, and these are represented in Figs. 8 and 9. From Fig. 8, it is clear that arc fault current amplitudes decrease with respect to irradiation level. Similarly, the voltages of utility disturbances also decrease their amplitude with respect to irradiation, as shown in Fig. 8.

All these variations of fault signals are passed through CUSUM for detection. The CUSUM method identifies abrupt changes that occurred in the input signal; because of this phenomenon, CUSUM is used to detect faults and disturbances. Here, the threshold is a user-defined value, and it is chosen as greater than 2 for detecting the faults, because at this threshold value, both arc faults and PQ disturbances can be detected accurately. If the results of the CUSUM exceed the predefined threshold, that instant of

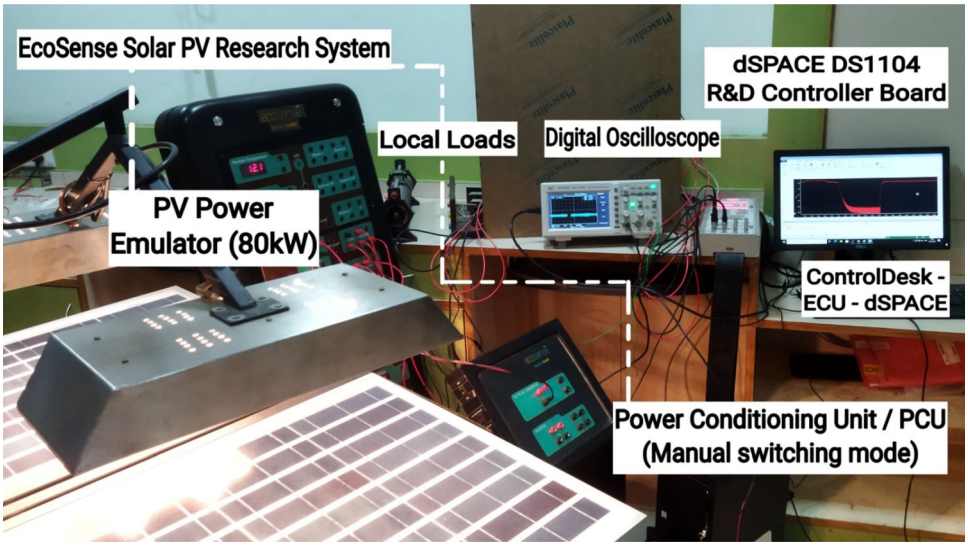

Fig. 20 Validation of PV-DG on hardware test bench setup using dSPACE DS1104

time is the fault detection time. Here, the threshold of each fault is indicated with the dotted line.

All the simulated fault signals (i.e., arc faults and utility disturbances) under different PV irradiation levels such as 100%, 75%, and 50% are detected using the CUSUM method, and these are represented in Figs. 10, 11, 12, 13, 14, and 15. The detection time of every fault is calculated under three variations, thus its average time is considered as the fault detection time, as reported in Table 2. Fault detection time is calculated by subtracting the CUSUM detection time to the actual fault-created time (1.2 s) for every variation.

Here, arc faults and utility disturbances are detected in less than 14 ms using the CUSUM method. Further, these detected signals are fed to the proposed classifier, i.e., OMW-VMD-MFDFA, for fault classification.

The initial step is set to 1, and $N - s + 1$ segments will be obtained for each iteration of the s using the OMW method. The next step is to perform the VMD operation for the decomposition of the $N - s + 1$ segments into IMFs, which are obtained from the OMW method. In order to reduce the computational burden of the proposed classifier, it is necessary to select the best IMF among the series of IMFs. Thus, the WKI is introduced in this work for selecting the best IMFs. By utilizing a threshold, three sensitive IMFs were selected out of a series of IMFs, shown in Figs. 16 and 17.

The IMF having the maximum value of WKI is treated as the IMF1 irrespective of the model number. Similarly, IMF2 and IMF3 are selected in the same manner. This approach is used to fit the polynomial by estimating the local trends instead of the least-square polynomial fitting method. VMD has several advantages over other existing techniques, such as sampling, noise elimination, end effect, and mode mixing; thus, VMD is preferred in this paper.

The proposed algorithm, i.e., OMW-MFDFA, is different from the basic MFDFA, and it provides the solution for any order of the polynomial function. In this approach, the fluctuation function $[Fq(s)]$ is calculated for differential fault current signals and power quality disturbances, with

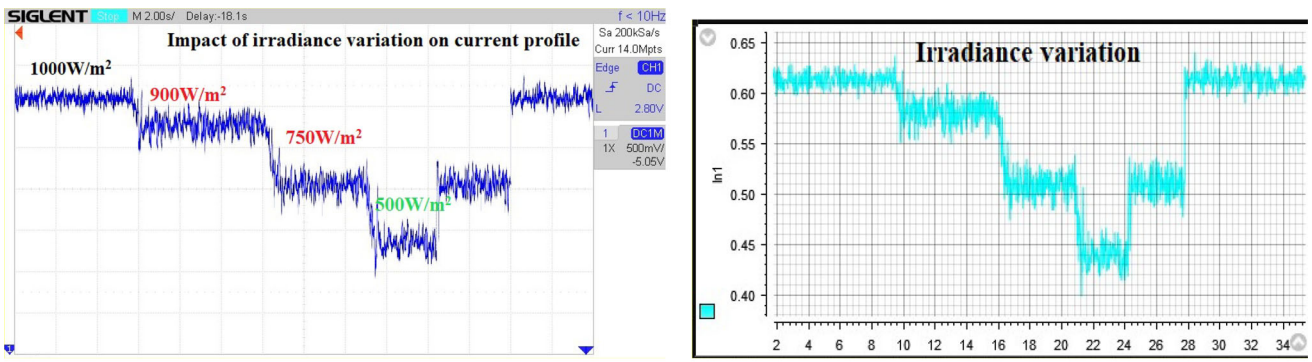

(a) (b)

Fig. 21 Validation of PV-DG during an arc fault: **a** uncertainty of PV irradiance; **b** corresponding output in Control Desk

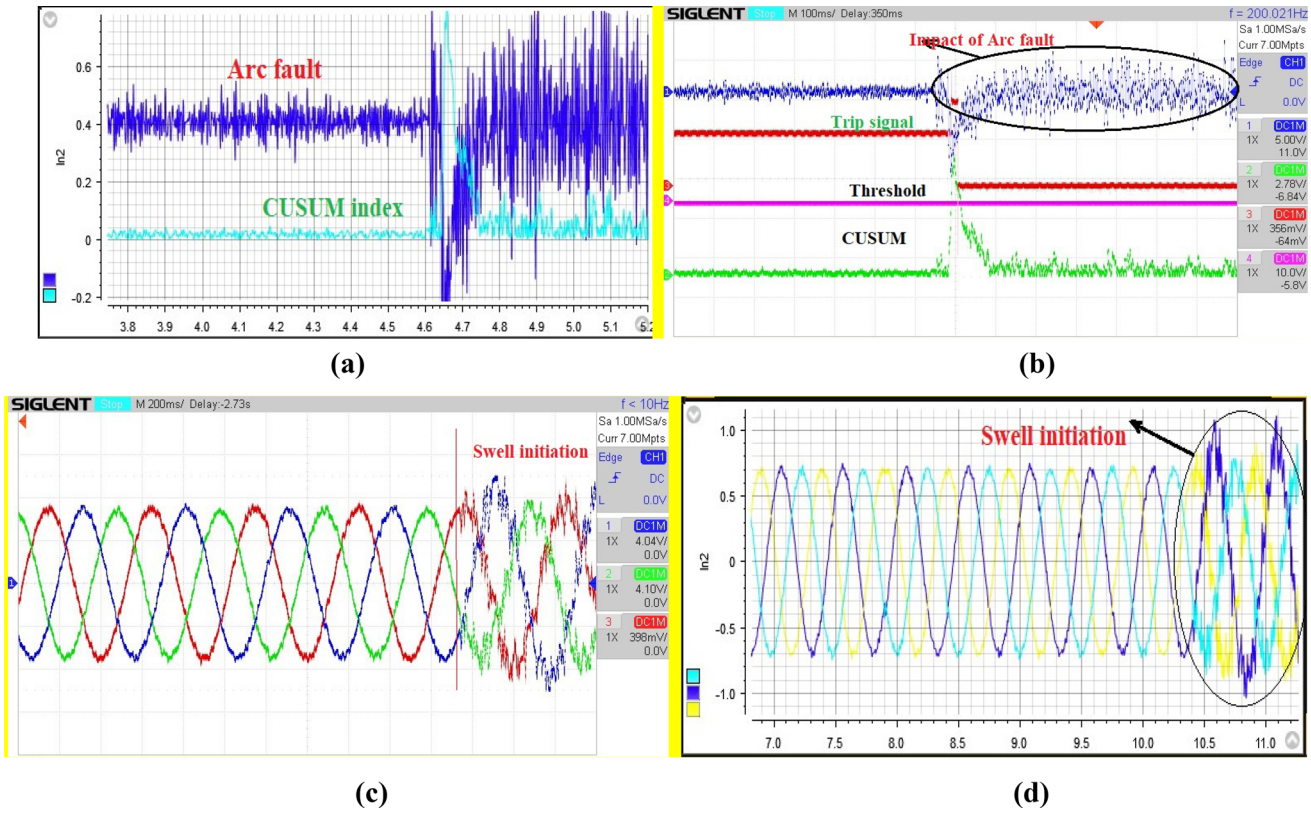

Fig. 22 Validation of arc faults and utility disturbances: **a** shunt-intra string arc fault in Control Desk; **b** corresponding output in a digital oscilloscope; **c** sag in a digital oscilloscope; and **d** corresponding output in Control Desk

different q values. To examine the nonlinear characteristics of the signal, three vectors (Hq, Mq, and Sq) were analyzed based on existing literature, and the most effective feature was found to be the Hurst exponent. This is due to the fact that when Hq exhibits long-range correlation, the log-linear fluctuation function of the signal displays power-law correlations, providing valuable insight into its nonlinear behavior (Anjaiah et al. 2022a).

In this paper, the authors investigated the nonlinear characteristics of differential fault current signals by varying the Hq and q values over a range of -5 to 5. Notably, a q value of 2.5 produced discriminative behavior in Hq when exposed to simulated arc faults and power quality disturbances, suggesting that Hq could serve as a reliable discriminator of nonlinear signal dynamics. Conversely, the Hq was rendered ineffective with $q = 0.3$, as it demonstrated inadequate selectivity and superimposed the fault signals. The scaling features of the fluctuation function are greater if the q and Hq variables are positive and less if they are negative. All of the aforementioned characteristics of the Hurst exponent are discernible within the range of $0.5 < Hq < 6.8$, as illustrated in Fig. 18a. A distinct classification between the scaling exponent (Mq) and q is evident from the plot, with the relationship between Mq and q displaying a nonlinear and convex-shaped curve, as depicted in Fig. 18b. Furthermore, Fig. 18c represents a multifractal spectrum whose shape resembles an inverted parabola. This spectrum exhibits truncated right tail and left tail features, indicating that arc faults and power quality disturbances are multifractal and possess internal dynamic characteristics. When it comes to fault signals, right tail properties exhibit insensitivity to local fluctuations due to their high magnitude, whereas the left tail properties exhibit insensitivity to local fluctuations due to their low magnitudes. Moreover, simulated faults have been distinguished at $\delta q = 2.5$ in the multifractal spectrum, as shown in Fig. 18c. Here, it is clear that increasing q and Hq results in a decrease in nonlinearity. Conversely, increasing q and Mq leads to an increase in nonlinearity. The nonlinearity, higher degree, and fluctuations in the fault signal are denoted not only by Hq but also by Mq and Sq.

5.3 A. Performance evaluation

To substantiate the efficacy of the proposed method, classification accuracy (CA) and relative computational time (RCT) (Prasad and Dash 2021) are used as metrics. The CA and RCT values obtained for the OMW-VMD-MFDFA method are as follows:

$$\text{Classification Accuracy (CA) \%} = \frac{\text{Truely classified features data samples}}{\text{Randomly chosen feature data samples from whole data}} \times 100 \quad (39)$$

$$\text{Relative computational time (RCT)} = \frac{\text{particular method computational time}}{\text{low computational time of overall methods}} \quad (40)$$

In this work, a total of five features such as Hq, Sq, δ_{max}, $\delta_{peak,}$ and $\Delta\delta_q$ are considered to analyze the classification accuracy of the proposed method. Except for Hq and $\underline{Sq}$, all the features are numeric; in order to obtain numerical values for Hq and $\underline{Sq}$ feature vectors, their mean is considered. A total of six kinds of faults are simulated from the proposed model. From these fault signals, the abovementioned features are extracted using the proposed OMW-VMD-MFDFA method and are reported in Table 3. A total of 180 variations are obtained for all the faults by considering different operating conditions, i.e., partial shading and solar irradiation. A total of 150 samples are randomly selected from the 180 samples to perform the classification of the fault. Out of randomly selected 150 samples, a total of 149 samples are classified exactly. Misclassification happens between swell and shunt cross-string arc faults, and they are observed from Fig. 19 in three dimensions. From Fig. 19, it is clear that out of five features, the combinations of Hurst exponent (Hq), singularity spectrum ($\underline{Sq}$), and spectrum width ($\Delta\delta_q$) show the accurate classification as compared to other combinations (i.e., Fig. 19a), and its CA is reported in Table 4. The other two sets are misclassified more compared to Fig. 19a.

Therefore, the combination of this feature set is considered to be the most optimal for analyzing nonlinear fault classification. To compute the CA and RCT, Eqs. (39) and (40) were employed, respectively. Moreover, the proposed OMW-VMD-MFDFA classifier is compared against benchmark techniques, such as DFA, MFDFA, adaptive MFDFA, OMW-MFDFA, and OMW-EEMD-MFDFA classifiers, to demonstrate its superiority in terms of CA and RCT.

Interestingly, Table 5 shows the superiority of the proposed classifier in terms of CA and RCT for the classification of arc faults and utility disturbances in the multiple PV-based DC ring microgrid. Even though the proposed methods (i.e., CUSUM**,** OMW-VMD-MFDFA) achieved outstanding performance, they have a few limitations, such as the difficulty in the selection of the threshold in the CUSUM method whenever fault current magnitude is much lower under a high-impedance scenario. Similarly, OMW-VMD-MFDFA also needs to be improved in terms of the selection of modal numbers and penalty factors for estimating the unknown trends, to obtain more accuracy in real-time applications.

5.4 Validation of the Proposed Method Through HIL Setup

This paper presents a hardware-in-loop (HIL) setup for a DC ring bus system that uses multiple photovoltaic (PV) sources and accommodates local loads, as illustrated in Fig. 20. The proposed OMW-VMD-MFDFA algorithm is intended for real-time applications in electrical engineering. To this end, we used an 80-W PV emulator and a DC–DC converter. The PV panels belong to ELDORA and have a rating of 40 W/panel. To obtain the maximum power (i.e., V_{MPP} and I_{MPP} of 17.9 V and 2.3A, respectively), we created artificial irradiance using 1.8-kW halogen bulbs mounted on top of the panel. We also installed a knob to vary the illumination, allowing us to validate the setup for partial shading and DG disconnections and to estimate the proposed algorithm's efficacy.

To extract and monitor the maximum PV power, we used PV Ecosense® and power conditioning units (PCU: 25-W DC–DC/50-W DC–AC operations) (Anjaiah et al. 2022b). We interfaced the real-time setup with dSPACE DS1104 using Tektronix® TPP0101 oscilloscope probes. The DS 1104 R&D control board, which runs at 250 MHz, is the master controller that performs analog-to-digital (ADC) and digital-to-analog (DAC) conversion at a switching frequency of 10 kHz (< rated 250 MHz). To implement the control logic for the converter, we used MATLAB/Simulink via the RTI library and Control Desk. We used 50-W resistive–inductive loads to achieve demand–supply balance.

5.5 Case 1: Impact of PV Irradiance Variation on Current

In order to verify the effectiveness of the proposed approach, the above designed HIL setup is utilized to test the proposed approach, which included 80-W generation. Irradiance was varied by adjusting the halogen lamps' luminance, with the maximum luminance set at 1000 W/m2, producing the rated output power for ELDORA PV panels. To validate uncertainty in PV, irradiance was varied from 1000 W/m2 to 500 W/m2. In real time, luminance was maintained at 1000 W/m2 until t = 10 s and then varied at t = 16 s, t = 21 s, t = 24 s, and t = 28 s. At t = 21 s, 40W of the ELDORA PV panel is completely turned off. To observe the impact of irradiance on the current profile, a digital oscilloscope is utilized, and its output is shown in Fig. 21a. For more effective representation, Control Desk output is also included in this paper, as shown in Fig. 21b.

5.6 Case 2: Fault Disturbance Detection using CUSUM in a Real-Time Environment

Further, to validate the proposed methodology, in the hardware setup, out of various discussed faults, a series arc fault is created with proper precautions. Here, the current profile is considered to detect the fault, since during an arc fault, voltage is nearly more than 10 times the normal voltage. To mitigate this fault, CUSUM logic is developed in dSPACE DS1104. Whenever the CUSUM index of the current profile exceeds the predefined threshold, it issues the trip signal to the circuit breaker for isolating the fault. To observe this phenomenon more effectively, the outcomes of the digital oscilloscope and Control Desk are represented in Fig. 22a, b. From Fig. 22a, it is clear that the arc fault is initiated at $t = 4.6$ s, and its corresponding CUSUM index peak is represented at $t = 4.65$ s. From Fig. 21b, we can observe that the trip signal is issued when the CUSUM_predefined threshold is exceeded.

Also, among various discussed utility disturbances, the impact of swell is observed in a real-time environment, which is caused by the sudden disconnection of load from the proposed test bench setup. This phenomenon can be observed in digital oscilloscope and Control Desk outcomes, as shown in Figs.22c and d, respectively.

6 Conclusion

In this paper, arc fault and utility disturbance detection and classification is carried out using a CUSUM-based improved MFDFA approach. Initially, arc fault and utility disturbance signals are recorded at the PCC in the proposed DC microgrid under PV partial shading and variable solar irradiation conditions. These signals are fed to the CUSUM method for fault detection. In this method, the instant at which CUSUM results exceed the threshold (i.e., > 2) is considered the fault detection point. All the simulated faults (i.e., arc faults and PQ disturbances) are detected in less than 14 ms using the CUSUM method. Further, these signals are fed to the improved MFDFA for classification. In this algorithm, stage 1 is based on the OMW method, and it is used to divide the profile into non-overlapping windows with equal lengths, and VMD is applied to decompose the segments of the OMW output into IMFs in stage 2. Also, the VMD algorithm is used for fitting the polynomial by estimating local trends with the help of the best three selected IMFs based on the maximum value of WKI. Finally, the proposed algorithm, i.e., OMW-VMD-MFDFA, is used for fault classification and to visualize the misclassification among the considered faults. A total of five distinct multifractal features are extracted from the proposed algorithm. From these features, suitable combinations are plotted in a three-dimensional scatter plot to show the distinct nature among the fault classes. Among these combinations, the Hurst exponent (Hq), singularity spectrum (Sq), and singularity spectrum width ($\Delta\delta_q$) combination showed more classification accuracy. Therefore, the following are the primary contributions and novelties of this paper.

(i) A DC ring microgrid based on multiple PV sources was constructed, and simulations of utility disturbances and arc faults were performed using a MATLAB/Simulink platform.
(ii) The CUSUM algorithm detects the captured signals of arc faults and utility disturbances in less than 14 ms.
(iii) The proposed classifier shows superiority in terms of CA and RCT over DFA, MFDFA, adaptive MFDFA, OMW-MFDFA, and OMW-EEMD-MFDFA classifiers with the assistance of best feature set such as Hq, Sq, and $\Delta\delta_q$ from the 3-D cluster graphs. The achieved classification accuracy is 99.33%, and the relative computational time is 1 p.u.
(iv) The dSPACE 1104 embedded processor implementation results in the MATLAB/Simulink environment prove the robustness, simplicity, and outstanding ability to recognize the different DC fault conditions using the proposed method over other state-of-the-art methods.

In light of the discussions, it is concluded that the OMW-VMD-MFDFA approach is more appropriate for fault detection and classification in a multi-PV-based DC ring microgrid, as compared to benchmark techniques.

References

Ahmad R, Murtaza AF, Sher HA, Shami UT, Olalekan S (2017) An analytical approach to study partial shading effects on PV array supported by literature. Renew Sustain Energy Rev 74:721–732

Ahmed J, Salam Z (2015) An improved perturb and observe (P&O) maximum power point tracking (MPPT) algorithm for higher efficiency. Appl Energy 150:97–108

Anjaiah K, Dash PK, Sahani M (2022a) A new protection scheme for PV-wind based DC-ring microgrid by using modified multifractal detrended fluctuation analysis. Protect Control Mod Power Syst 7(1):8

Anjaiah K, Dash PK, Sahani M (2022b) Detection of faults and DG islanding in PV-Wind DC ring bus microgrid by using optimized VMD based improved broad learning system. ISA Trans 131:533–551

Augustine S, Reno MJ, Brahma SM, Lavrova O (2020) Fault current control and protection in a standalone DC microgrid using

adaptive droop and current derivative. IEEE Journal of Emerging and Selected Topics in Power Electronics. 9(3):2529–2539
Chatterjee S, Pratiher S, Bose R (2017) Multifractal detrended fluctuation analysis based novel feature extraction technique for automated detection of focal and non-focal electroencephalogram signals. IET Sci Meas Technol 11(8):1014–1021
Cho SH, Shin HC, Lee JB, Jung HS, Shin SK (2019) An effective detection method of voltage and frequency fluctuations based on a combination of TEO/DESA and STFT analysis. J Electrical Eng Technol 14(2):985–991
Das S, Pradhan AK, Kedia A, Dalai S, Chatterjee B, Chakravorti S (2018) Diagnosis of power quality events based on detrended fluctuation analysis. IEEE Trans Industr Electron 65(9):7322–7331
Dhar S, Patnaik RK, Dash PK (2017) Fault detection and location of photovoltaic based DC microgrid using differential protection strategy. IEEE Trans Smart Grid 9(5):4303–4312
Dhar S, Dash PK (2017) Differential current-based fault protection with adaptive threshold for multiple PV-based DC microgrid. IET Renew Power Gener 11(6):778–790
Gajula K, Herrera L (2020) Detection and localization of series arc faults in dc microgrids using kalman filter. IEEE J Emerg Selected Top Power Electronics. 9(3):2589–2596
Gu R, Chen J, Hong R, Wang H, Wu W (2020) Incipient fault diagnosis of rolling bearings based on adaptive variational mode decomposition and Teager energy operator. Measurement 149:106941
Isham MF, Leong MS, Lim MH, Ahmad ZA (2018) Variational mode decomposition: mode determination method for rotating machinery diagnosis. J Vibroeng 20(7):2604–2621
Justo JJ, Mwasilu F, Lee J, Jung JW (2013) AC-microgrids versus DC-microgrids with distributed energy resources: a review. Renew Sustain Energy Rev 24:387–405
Kurniawan A, Shintaku E (2020) A neural network-based rapid maximum power point tracking method for photovoltaic systems in partial shading conditions. Appl Solar Energy 56:157–167
Lala H, Karmakar S (2020) Detection and experimental validation of high impedance arc fault in distribution system using empirical mode decomposition. IEEE Syst J 14(3):3494–3505
Lin J, Dou C, Liu Y (2021) Multifractal detrended fluctuation analysis based on optimized empirical mode decomposition for complex signal analysis. Nonlinear Dyn 103(3):2461–2474
Liu Z, Cui Y, Li W (2015) A classification method for complex power quality disturbances using EEMD and rank wavelet SVM. IEEE Trans Smart Grid 6(4):1678–1685
Mahela OP, Shaik AG (2017) Power quality recognition in distribution system with solar energy penetration using S-transform and Fuzzy C-means clustering. Renew Energy 106:37–51
Mahela OP, Shaik AG, Gupta N, Khosravy M, Khan B, Alhelou HH, Padmanaban S (2020) Recognition of Power Quality Issues Associated With Grid Integrated Solar Photovoltaic Plant in Experimental Framework. IEEE Syst J 15:3740–3748
Martínez JLM, Segovia-Domínguez I, Rodríguez IQ, Horta-Rangel FA, Sosa-Gómez G (2021) A modified multifractal detrended fluctuation analysis (MFDFA) approach for multifractal analysis of precipitation. Phys A 565:125611
Miao Y, Zhao M, Lin J (2019) Identification of mechanical compound-fault based on the improved parameter-adaptive variational mode decomposition. ISA Trans 84:82–95
Mohanty R, Pradhan AK (2018) DC ring bus microgrid protection using the oscillation frequency and transient power. IEEE Syst J 13(1):875–884
Musa MH, He Z, Fu L, Deng Y (2018) A cumulative standard deviation sum based method for high resistance fault identification and classification in power transmission lines. Protect Control Mod Power Syst 3(1):1–12
Naik J, Dhar S, Dash PK (2019) Adaptive differential relay coordination for PV DC microgrid using a new kernel based time-frequency transform. Int J Electr Power Energy Syst 106:56–67
Noori MR, Shahrtash SM (2013) Combined fault detector and faulted phase selector for transmission lines based on adaptive cumulative sum method. IEEE Trans Power Delivery 28(3):1779–1787
Pragathi B, Poonia RC, Polaiah B, Nayak DK (2021) Evaluation and Analysis of Soft Computing Techniques for Grid Connected Photo Voltaic System to Enhance Power Quality Issues. J Electrical Eng Technol 16:1–8
Prasad EN, Dash PK (2021) Fault analysis in photovoltaic generation based DC microgrid using multifractal detrended fluctuation analysis. Int Trans Electrical Energy Syst 31(1):e12564
Saleh M, Esa Y, Mohamed AA (2018) Communication-based control for DC microgrids. IEEE Trans Smart Grid 10(2):2180–2195
Sarangi S, Sahu BK, Rout PK (2020) Distributed generation hybrid AC/DC microgrid protection: A critical review on issues, strategies, and future directions. Int J Energy Res 44(5):3347–3364
Shaikh A, Shaikh PH, Kumar L, Mirjat NH, Memon ZA, Assad MEH, Alayi R (2022) Design and modeling of a grid-connected PV–WT hybrid microgrid system using net metering facility. Iran J Sci Technol Trans Electrical Eng 46(4):1189–1205
Subasi A, Yilmaz AS, Tufan K (2011) Detection of generated and measured transient power quality events using teager energy operator. Energy Convers Manage 52(4):1959–1967
Ullah MF, Hanif A (2021) Power quality improvement in distribution system using distribution static compensator with super twisting sliding mode control. Int Trans Electrical Energy Syst 31:e12997
Wang Z, Balog RS (2015) Arc fault and flash signal analysis in DC distribution systems using wavelet transformation. IEEE Trans Smart Grid 6(4):1955–1963
Xiong Q, Ji S, Zhu L, Zhong L, Liu Y (2017) A novel DC arc fault detection method based on electromagnetic radiation signal. IEEE Trans Plasma Sci 45(3):472–478
Xu Y, Gao Y, Li Z, Lu M (2019) Detection and classification of power quality disturbances in distribution networks based on VMD and DFA. CSEE J Power Energy Syst 6(1):122–130
Yao X, Herrera L, Ji S, Zou K, Wang J (2013) Characteristic study and time-domain discrete-wavelet-transform based hybrid detection of series DC arc faults. IEEE Trans Power Electron 29(6):3103–3115
Yao X (2016) Study on DC arc faults in ring-bus DC microgrids with constant power loads. In: 2016 IEEE energy conversion congress and exposition (ECCE) (pp 1–5). IEEE
Zhang X, Zhang G, Qiu L, Zhang B, Sun Y, Gui Z, Zhang Q (2019) A modified multifractal detrended fluctuation analysis (MFDFA) approach for multifractal analysis of precipitation in dongting lake basin, China. Water 11(5):891